Geothermics 127 (2025) 103262

Contents lists available at ScienceDirect

Geothermics

journal homepage: www.elsevier.com/locate/geothermics

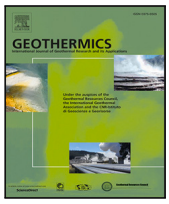

Impact of land cover and climate change on Aquifer Thermal and Energy Storage (ATES) system performance

Godinaud Jérémy [a,*], Pryet Alexandre [a], Bayer Peter [b], Larroque François [a]

[a] Univ. Bordeaux, CNRS, Bordeaux INP, EPOC, UMR 5805, Pessac, 33600, France
[b] Martin Luther University Halle-Wittenberg, Applied Geology, Von-Seckendorff-Platz 3 Halle/Saale, 06120, Germany

ARTICLE INFO

Keywords:
ATES
SUHI
Climate change
Ground Surface Temperature

ABSTRACT

This study investigates the impact of climate change and intense urbanization on Low-Temperature Aquifer Thermal Energy Storage (LT-ATES) systems. A synthetic groundwater model was developed to consider transient thermal boundary conditions due to climate change, urbanization, and evolving building thermal demands. Four scenarios were analyzed, showing potentially significant influences on subsurface thermal conditions, leading to distinct aquifer temperature profiles. The results for conditions with strong ground heat gain indicate pronounced subsurface warming and imbalanced thermal plume extensions and decreasing ATES performance over time. Recommendations include incorporating realistic surface boundary conditions in ATES modeling and strategies to mitigate adverse thermal impacts from urbanization.

1. Introduction

Low Temperature (<25 °C) Aquifer Thermal Energy Storage (LT-ATES) is an open-loop geothermal system based on seasonal thermal energy storage in an aquifer. It uses two different groups of wells ("cold" and "warm") to store and extract seasonally cold and warm water from an aquifer to provide thermal energy to buildings. The thermal energy is transferred from the pumped water to the building through a heat exchanger (Fig. 1). ATES operation can lower both the cost and environmental impact of regulating building temperatures compared to traditional fossil fuel-based systems (Godinaud et al., 2024; Stemmle et al., 2021; Moulopoulos, 2014).

The performance of ATES is mainly assessed with two criteria: storage efficiency and abstraction temperature (Fleuchaus et al., 2019). These criteria are met by optimizing ATES design with respect to energy demand and hydrogeological conditions. Therefore, in practice, special attention is given to the influence of aquifer parameters' heterogeneity or natural groundwater velocity on storage efficiency and thermal plume extension (Ferguson, 2007; Bridger and Allen, 2014; Visser et al., 2015; Bloemendal and Hartog, 2018; Bloemendal and Olsthoorn, 2018).

ATES systems are particularly suitable to provide heat and cold to urban districts (Rostampour et al., 2019) or large buildings such as office buildings (Kranz and Frick, 2013), airports (Baxter et al., 2018), hospitals (Vanhoudt et al., 2011; Schüppler et al., 2019), and universities (Behi et al., 2014). Surface artificialization of cities (buildings, roads, car parks) and underground constructions (car parks, tunnels, subways) modify soil, surface, and ground thermal properties, generating a surplus energy transfer to the subsurface (Noethen et al., 2023). The heat accumulation in the ground is responsible for a temperature increase often reaching between 2 °C and 6 °C compared to undistributed rural areas, which manifests as a Subsurface Urban Heat Island (SUHI) (Ferguson and Woodbury, 2004; Bayer et al., 2019; Blum et al., 2021; Watson and Westaway, 2020). Indeed, in urban environments, borehole measurements show a typical log C-shaped temperature distribution, and the geothermal gradient appears to approach its typical value below 100–150 m depth. The evolution of SUHIs causes the accumulation of substantial energy in the shallow ground and groundwater (Attard et al., 2016; Visser et al., 2020; Epting et al., 2021). For example, in the cities of Milan (Italy), Cologne (Germany), and Karlsruhe (Germany) 1.0, 1.4 and 2.1 PJ y^{-1}, respectively, are transferred to the underground (Benz et al., 2015; Previati et al., 2022). Thus, SUHIs present a high potential to develop geothermal activities for heating purposes. In Karlsruhe and the western part of Cologne, the stored energy would be sufficient to sustainably cover 32% and 9%, respectively, of annual residential space heating demand Benz et al. (2015). A case study in a district of London also demonstrates that 50% of the total heat demand could be supplied by geothermal extraction using SUHI benefits (Bidarmaghz et al., 2021). Including the effect of continued global ground warming, Benz et al. (2022) showed that at least 97% of the 8000 sites they used in their study would be

* Corresponding author.
E-mail address: jeremy.godinaud@bordeaux-inp.fr (G. Jérémy).

https://doi.org/10.1016/j.geothermics.2025.103262
Received 28 May 2024; Received in revised form 16 December 2024; Accepted 19 January 2025

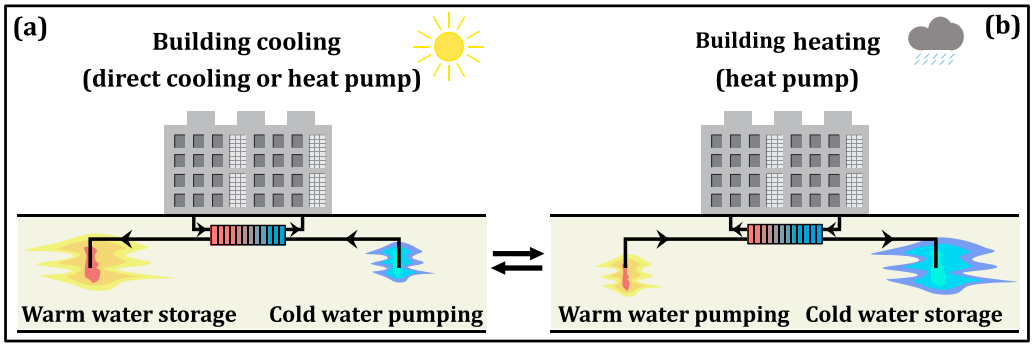

Fig. 1. Operation of an LT-ATES system: (a) in summer, cold water is extracted from the aquifer, and this cools down the building either directly (free-cooling) or with a heat pump; (b) in winter, the stored warm water is extracted from the aquifer, and a heat pump is required to reach a suitable temperature for heating the building.

suitable to use the subsurface heat recycling to fulfill heating demand by considering climate change projection RCP8.5 by the end of the 21th century. Nevertheless, cold production also plays a key role in ATES operation, and to our knowledge, only Arola and Korkka-Niemi (2014) address the impact of SUHI on cold extraction with geothermal systems. They demonstrate that in southern Finnish cities, the SUHI effect generates a reduction of 50% of peak cooling power.

As noted by Fleuchaus et al. (2019), the impact of the SUHI effect on the performance of ATES systems has not been previously investigated. Typically, the performance of ATES systems is analyzed using an initially uniform aquifer temperature, even when a SUHI influences the aquifer. To our knowledge, only Visser et al. (2015) consider land cover and historical surface changes in their modeling of an ATES system. They demonstrated the necessity of including these parameters to model a vertical temperature distribution that closely matches the observed temperature at an ATES site before the start of operations—a crucial step for accurate thermal impact assessment of ATES. In their study, they also coupled the effects of land use and aquifer heterogeneity on the thermal plume extension of ATES. They aimed to compare their model results with the temperature distribution monitored from boreholes. However, they did not perform model projections to evaluate the impact of these parameters on ATES performance during long-term operation.

Moreover, with the atmospheric temperature increase induced by climate change, the thermal demand for buildings is expected to change during the 21st century (Alves et al., 2021; Ciancio et al., 2020; Jalali et al., 2023; Reveshti et al., 2023). The intensity of these changes is under discussion, but the global trend is an increase in the cooling load and a decrease in the heating load. For ATES systems, this may yield an over-pumping of the cold well resulting in a surplus of heat storage in the aquifer during summer. On the contrary, during winter, cold water storage may decrease due to the heating load reduction of buildings. Considering the climatic projection of the A1Fl scenario (projected to continue to have strong growth in fossil fuel production) in 2050–2075, Bloemendal et al. (2015) demonstrated that about 3% of the world's urban population will live in areas with high suitability for ATES application, while it was 15% at the end of the 20th century. Overall, climate change should reduce cold availability in aquifers, while the building cooling load is expected to increase. Bozkaya et al. (2018) stressed the importance of reaching a thermally balanced building to optimize ATES performance. Nevertheless, the potential changes in the thermal balance of buildings and aquifers for ATES systems have not been investigated in detail under the progression of climate change.

This study aims to assess the performance (storage efficiency) and thermal plume extension of a synthetic ATES system considering both SUHI and climate change effects on building thermal load. This is examined through numerical model simulations of synthetic ATES configurations influenced by urban thermal conditions, with four distinct scenarios developed for this analysis. The focus is on illuminating how extreme conditions applied to the Ground Surface Temperature (GST) and building thermal demand influence ATES performance. Exploring extreme conditions allows us to get an insight into the range of possible conditions and cases. The first part of the paper presents the studied scenarios and the construction of the numerical model used to solve hydrodynamic and thermal transfer equations in the aquifer. The second part details and compares the results of the different scenarios.

2. Methods

2.1. Definition of GST scenarios

This study is based on a theoretical case oriented at the city of Bordeaux (France). We focus on a doublet ATES system with one cold and one warm well, which are operated in a confined aquifer at a depth between 20 m and 55 m. The target below the 20 m depth prevents the influence of seasonal atmospheric temperature fluctuations on groundwater temperature (Taylor and Stefan, 2009). The ATES aims to provide thermal energy (warm and cold) to an office building of 15,000 m^2 accommodating 650 workers. The operation of the ATES starts in 2022 with a duration of 60 years. To examine the influence of climatic conditions and land use change on ATES performance, four distinct scenarios (Table 1) considering different climatic conditions pre- and post-2022 in the city of Bordeaux (Fig. 2a) and the extent of urbanization in the same city are tested.

Scenarios 1 and 2 do not consider the impact of urbanization. For the urbanization scenarios 3 and 4, the process started in 1990 with simultaneous development of the entire area. The land use patterns (Fig. 2b) in scenarios 3 and 4 were retrieved from a geographic information system software (QGIS) assessment of the city of Bordeaux, corresponding respectively to the university campus area (Fig. 2c) and the city center (Fig. 2d).

Scenarios 2, 3, and 4 encompass the historical Surface Atmospheric Temperature (SAT) evolution (Fig. 3), whereas scenario 1 depicts a static temperature set at the 2022 value in Bordeaux, serving as a reference scenario frequently employed to model the impact and performance of geothermal systems.

The past SATs were gathered from the meteorological station in Bordeaux-Mérignac (France), covering the period from 1906 to 2022. The data highlights a clear temperature increase in this city, representing the trend observed on a European scale. This rise started in the second part of the 20th century, resulting in present temperatures around 2.0 °C above temperatures measured in the first part of the 20th century. For scenarios 2, 3, and 4, the SAT values were retrieved using a local polynomial regression applied to the annual average temperature values before 2022 and the projected temperatures after 2022 (lines in Fig. 3). Since the current SAT in Bordeaux is already 2.0 °C higher than in 1900, we decided to use the projected temperature data from the RCP8.5 climate scenario for Bordeaux.

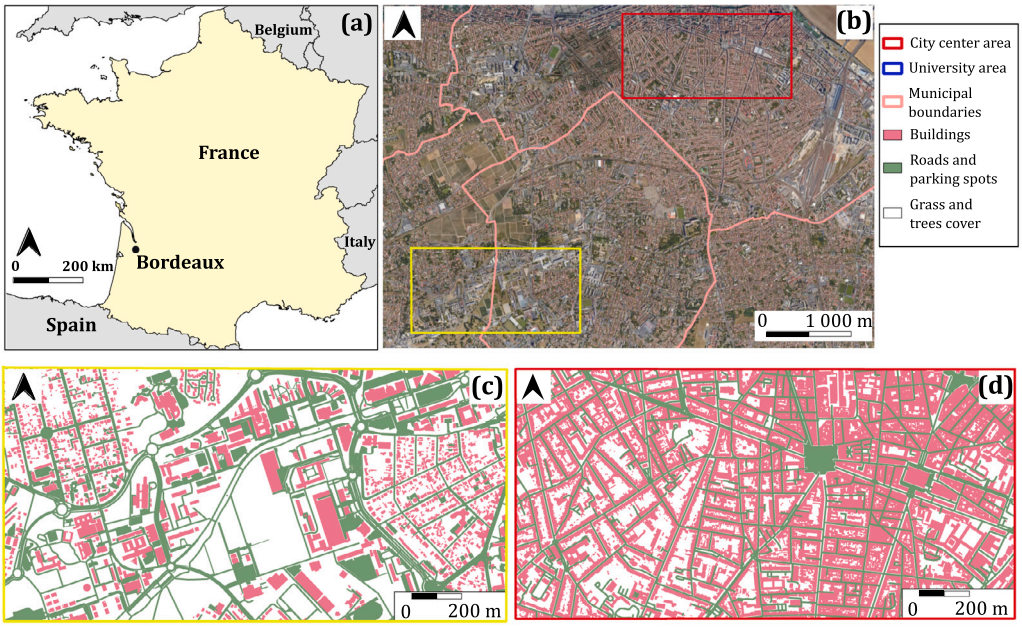

Fig. 2. Spatial conditions and land use: (a) location of Bordeaux in France, (b) location of the two areas of interest in the city, with the land use of (c) the university area and (d) the city center area.

Table 1
Climatic and urbanization trends for the four studied scenarios are detailed in the second column. In the last column, the abbreviations represent NL = Natural land, S = Streets and sideways, and B = Buildings.

Scenario	Surface Atmospheric Temperature (SAT) before 2022	SAT after 2022	Intensity of urbanization	Surface occupation share
1	Stable at 2022 value	Stable at 2022 value	No urbanization	NL :100%
2	Past Bordeaux SAT	RCP 8.5	No urbanization	NL :100%
3	Past Bordeaux SAT	RCP 8.5	Low urbanization	NL :56% S :26% B :18%
4	Past Bordeaux SAT	RCP 8.5	High urbanization	NL :25% S :25% B :50%

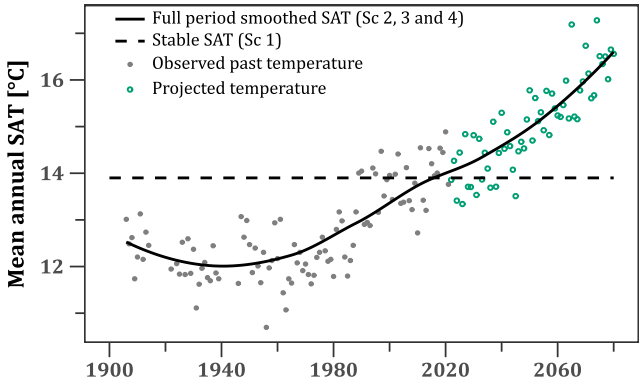

Fig. 3. Temperature observed at the Bordeaux-Mérignac weather station and projected value from RCP8.5 after 2022 (dots). The lines represent local polynomial regression adjustment considering RCP8.5 projection after 2022 (solid) or stabilization of the temperature after 2022 (dashed).

2.2. Definition of the GST

Past studies (Harris and Chapman, 1997; Huang et al., 2000; Ferguson and Woodbury, 2004; Bayer et al., 2016) have shown that historical trends in GST influence the distribution of borehole temperature logs in the first 100–150 m depth of the ground. The GST value is directly influenced by the SAT and urbanization/artificialization development. Following Rivera et al. (2015) the GST for natural land can be written as:

$$GST_{nat} = SAT + \Delta T_{S-A} \quad (1)$$

where SAT is the Surface Atmospheric Temperature and ΔT_{S-A} the difference between the SAT and the temperature at the surface of natural soil. This parameter depends on surface conditions such as wind, soil type, altitude, snow pack and evapotranspiration (Herb et al., 2008; Banks, 2012). In the city of Zurich (Switzerland), Bayer et al. (2016) found ΔT_{S-A} values ranging between 1.6 and 2.7 °C. Based on other results from Visser et al. (2015) and Godinaud (2023), a value of 1.0 °C is set for this study.

When the surface is covered with asphalt or equivalent material (streets or parking spots for example), Eq. (1) becomes:

$$GST_{asph} = SAT + \Delta T_{S-A} + \Delta T_a \quad (2)$$

where ΔT_a is the difference between the surface temperature of natural soils and the temperature at the surface of a soil covered with asphalt. According to Dědeček et al. (2012) and Bayer et al. (2016), a yearly average ΔT_a of 3–4 °C can be used.

Finally, GST below a building can be expressed as :

$$GST_{build} = T_b \quad (3)$$

where T_b represents a yearly average fixed surface temperature ranging between 15.0 and 20.0 °C (Rivera et al., 2015; Bayer et al., 2016; Benz et al., 2015). This temperature depends on the building envelope and thermal loss from the slab/floor. For this study, T_b = 19.0 °C is assumed. We chose this high value to account for significant urban subsurface warming also triggered by heat losses from further sources such as sewage leakage or district heating networks (Benz et al., 2015). Together with the climate scenario RCP8.5, this high heat loss allows us to focus on extreme conditions for urban subsurface heating and consequences for ATES performance.

For simplification, in the numerical groundwater model, we defined a uniform GST value of each area as the spatial average of surface

temperatures:

$$GST = \sum_i \beta_i \times GST_i \quad (4)$$

where GST_i is the temperature and β_i the relative coverage area, associated with the ith surface occupation share (natural land, streets, or buildings) (Table 1 and Fig. 2c and d).

2.3. Definition of pumped/injected volumes

Aside from ground temperature distribution, SAT influences building thermal load and thus pumped/injected volumes from/in the wells. For this study, the daily thermal load of the building is calculated following the ASHRAE methodology (ASHRAE, 1997, 2021) based on daily SAT projection. Appendix contains information on the building envelope parameters and the thermal load calculation specifics (Tables A.3,A.4, A.5 and A.6). Considering the thermal demand of the building, the required flow rate Q ($m^3\,h^{-1}$) from the warm well is expressed as:

$$Q_{warm} = \frac{P(1 - \frac{1}{COP})}{\Delta T \rho_w c_w} \quad (5)$$

and the required flow rate from the cold well during the cooling period is:

$$Q_{cold} = \frac{P(1 + \frac{1}{COP})}{\Delta T \rho_w c_w} \quad (6)$$

where COP (-) is the Coefficient Of Performance of the heat pump (i.e., the ratio between the useful produced thermal power and the required electricity to power the heat pump) in warm and cold mode (Bulté et al., 2021), ΔT (K) is the temperature difference between the upstream and downstream of the heat exchange, P (kW) is the thermal demand of the building, and $\rho_w c_w$ ($kW\,h\,m^{-3}\,K^{-1}$) the volumetric heat capacity of the water.

2.4. Setup of the numerical model

2.4.1. Groundwater flow and heat transport equation

The following equation represents the three-dimensional (3D) transient groundwater flow in saturated porous media:

$$-\nabla \cdot (-K \nabla h) + w = S_s \frac{\partial h}{\partial t} \quad (7)$$

with K ($m\,s^{-1}$) the hydraulic conductivity, S_s (m^{-1}) the specific storage, h (m) the piezometric head, t (s) the time, and w (s^{-1}) the sink.

The heat transport equation reads as follows:

$$v c_w \rho_w \cdot \nabla T - (\lambda_{bulk} + \alpha \cdot c_{bulk} \rho_{bulk} \cdot v) \cdot \nabla^2 T + c_{bulk} \rho_{bulk} \frac{\partial T}{\partial t} - s = 0 \quad (8)$$

with v ($m\,s^{-1}$) the vector of water flux, $c_{bulk}\rho_{bulk}$ and $c_w \rho_w$ ($J\,m^{-3}\,K^{-1}$) the volumetric heat capacity of the porous media and water, λ_{bulk} ($W\,m^{-1}\,K^{-1}$) the bulk thermal conductivity, and α (m) the thermal dispersivity. The latter is specified as α_L in the direction parallel to the water flow and as α_T in the direction perpendicular to the water flow (typically, α_T is set equal to 0.1 α_L). Finally, s ($W\,m^{-3}$) represents the heat source.

The low temperature variation along the modeled domain involved in this study allows us to ignore density and viscosity effects on heat transport modeling. Viscosity effects are considered negligible when the temperature difference across the model domain is less than 30 °C, and fluid density can be assumed constant when the maximum temperature difference across the model domain does not exceed 15 °C (Ma and Zheng, 2010).

Table 2
Thermal and hydrodynamic parameters used in the 3D model (i represents the imposed regional hydraulic gradient in the model domain.)

	K ($m\,s^{-1}$)	S_s (m^{-1})	i (%)	λ ($W\,m^{-1}\,K^{-1}$)	$c_s\rho_s$ ($MJ\,m^{-3}\,K^{-1}$)	α_L (m)
Aquifer	10^{-5}	10^{-4}	0.8	3.0	2.52	5.0
Aquitard	10^{-9}	10^{-4}	0.8	2.0	2.52	5.0

2.4.2. Conceptual and numerical model

The 3D-modeled domain constitutes a block centered around the building and the ATES system. It comprises one aquifer between 20 and 55 m depth confined between two low-permeability formations. The ATES wells, F1 and F2 (55 m depth), are separated by a distance of 150 m and set perpendicular to the groundwater flow direction to prevent thermal interaction between warm and cold thermal plumes (Fig. 4).

The domain extension is predetermined to restrict the interaction or influence of the Boundary Conditions (BCs) established at the borders and top and bottom faces. The BCs for groundwater flow simulation are:

- Along the west and east faces: imposed constant piezometric heads (Dirichlet BC) creating a 0.8% gradient (i) from west to east;
- on the top, bottom, north, and south faces: zero-flux BC;
- at the wells: imposed flux with a transient Neuman BC equal to the abstracted (+) or injected (−) calculated flow rate.

The heat transport BCs are the following:

- on the top face: transient Dirichlet BC representing the yearly average GST;
- on the bottom face: fixed temperature value (Dirichlet BC) to reproduce a geothermal gradient below the area of influence of surface temperature. Typical values range from 2–3.5 °C per 100 m (Banks, 2012). Here we chose a value of 3.0 °C per 100 m;
- on the west face (upgradient): depth-dependent transient Dirichlet BC. Prescribed temperatures were obtained from a simple, independent numerical model only accounting for heat diffusion along the vertical direction given transient GST;
- on the east face (downgradient): free BC heat flux;
- at the wells: transient Dirichlet temperature BC to maintain a constant temperature difference of 5.0 °C between the two wells.

The hydrodynamic and thermal equations are solved using the finite element method implemented in the software FEFLOW . The parameter values of the simulated porous media are depicted in Table 2.

The constant temperature difference of 5.0 °C between the two wells is implemented with the *OpenLoop* plug-in of the software. The mesh was refined around the two ATES wells (Fig. 4), and the model was vertically extended in 3D with 65 layers. [omment = to justify the layer number]Vertical refinement was applied near the surface and at geological unit interfaces to mitigate numerical instability arising from local property contrasts, featuring increased vertical refinement near the surface and at geological unit interfaces. This yields a mesh of about 297,000 elements. The aquifer is supposed to be fully confined, and therefore, the simulated aquifer layer is always saturated.

2.5. ATES performance analysis

For each scenario, based on Fleuchaus et al. (2019) and Sommer et al. (2013) the ATES wells' performance can be individually estimated for each cycle with:

$$\eta_i = \frac{\int_0^{t_{abs,i}} Q_{abs,i}(\tau)\Delta T_{abs,i}(\tau) d\tau}{\int_0^{t_{inj,i}} Q_{inj,i}(\tau)\Delta T_{inj,i}(\tau) d\tau} \quad (9)$$

where:

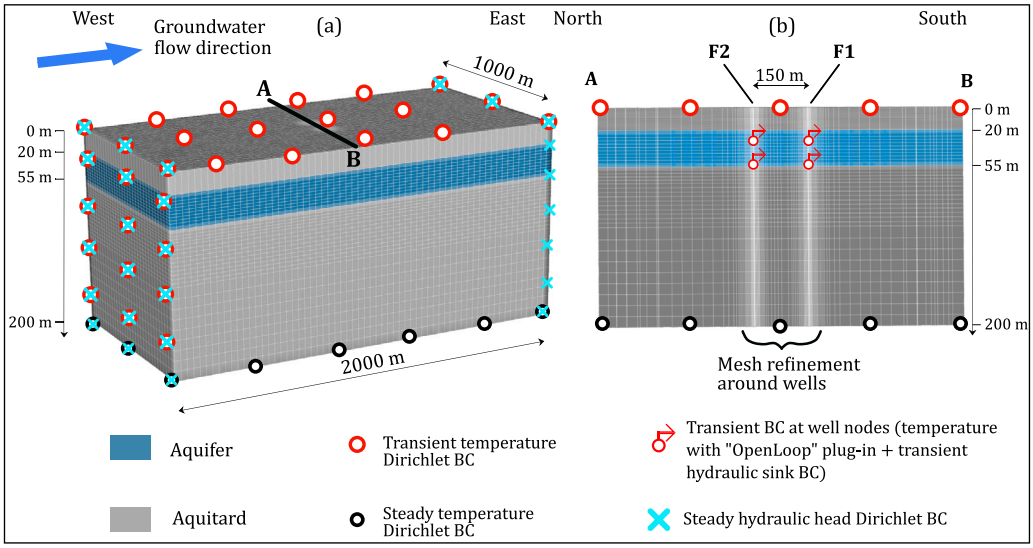

Fig. 4. (a) 3D mesh of finite elements with hydraulic and thermal boundary conditions (vertical exaggeration × 5.0), and (b) north–south vertical cross-section through the wells showing mesh local refinements (vertical exaggeration × 3.0).

- $t_{abs,i}$ and $t_{inj,i}$ (s) are the duration of the abstraction and injection phases, respectively.
- $Q_{abs,i}$ ($m^3\ s^{-1}$) represents the abstracted flow rate for one well and ($Q_{inj,i}$ $m^3\ s^{-1}$) the injected flow rate at the same well during the previous season.
- $\Delta T_{abs,i}$ and $\Delta T_{inj,i}$ (°C) represent the temperature difference of abstracted and injected water with T_{amb}, respectively.
- T_{amb} (°C) is the ambient groundwater temperature in the aquifer before ATES start-up.

If $Q_{abs,i}$ (τ) and $Q_{abs,i}$ (τ) are both constant throughout the ith cycle, we can introduce their average values over the cycle, $\overline{Q}_{abs,i}$ and $\overline{Q}_{inj,i}$, in Eq. (9) to get:

$$\eta_i = \frac{\overline{Q}_{abs,i}\int_0^{t_{abs,i}} \Delta T_{abs,i}(\tau)d\tau}{\overline{Q}_{inj,i}\int_0^{t_i nj,i} \Delta T_{inj,i}(\tau)d\tau} \quad (10)$$

We can then introduce the average temperature variations over the cycle:

$$\overline{\Delta T}_{abs,i} = \frac{1}{t_{abs,i}}\int_0^{t_{abs,i}} \Delta T_{abs,i}(\tau)d\tau \quad (11)$$

$$\overline{\Delta T}_{inj,i} = \frac{1}{t_{inj,i}}\int_0^{t_{inj,i}} \Delta T_{inj,i}(\tau)d\tau \quad (12)$$

So that Eq. (10) can be simplified as follows:

$$\eta_i = \frac{\overline{Q}_{abs,i}\times t_{abs,i}}{\overline{Q}_{inj,i}\times t_{inj,i}} \times \frac{\overline{\Delta T}_{abs,i}}{\overline{\Delta T}_{inj,i}} = \frac{V_{abs,i}}{V_{inj,i}} \times \frac{\overline{\Delta T}_{abs,i}}{\overline{\Delta T}_{inj,i}} \quad (13)$$

We eventually get:

$$\eta_i = R_{V,i} \times R_{T,i} \quad (14)$$

The derived indicators $R_{V,i}$ and $R_{T,i}$ allow consideration of:

- the dynamics of groundwater temperature evolution due to the thermal plume at the well;
- the dynamics of the building thermal load directly impacting the abstracted and pumped groundwater volumes from and into the aquifer.

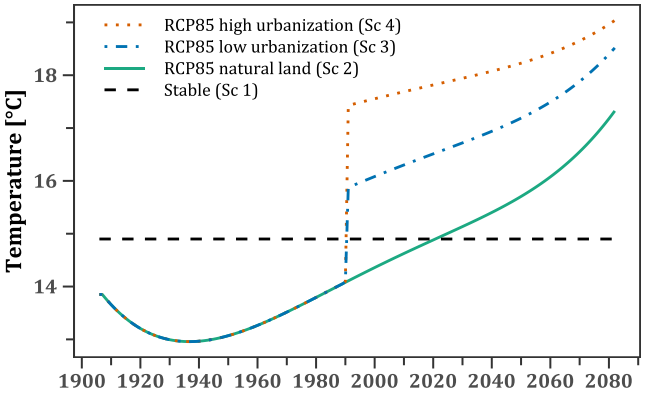

Fig. 5. GST modeled for each scenario. The sharp GST increase in scenarios 3 and 4 refers to the start of urbanization in 1990.

3. Results

3.1. Ground surface temperature simulation

For each scenario, a homogeneous annual average GST is generated (Fig. 5) using the SAT values in Fig. 3 and Eq. (4). Scenarios 3 and 4 account for urban development starting from 1990.

3.2. Projected pumped/injected volumes

The extracted/injected flow rates were calculated considering a heat pump presenting a COP of 5, a typical value reported for ATES in related studies (Vanhoudt et al., 2011; Gao et al., 2017; Schüppler et al., 2019; Luo and Ma, 2022). For simplicity, this value is supposed to remain constant in the heating and cooling mode. Following the analysis of 73 ATES in the Netherlands (Fleuchaus et al., 2019) a ΔT of 5.0 °C is defined. The daily flow rate is calculated (Eqs. (5) and (6)) based on daily thermal loads (Appendix) that are averaged for each cold and warm period. We consider a cooling period of 134 days and a warming period of 231 days. The corresponding annually extracted volumes are calculated using a local polynomial regression on

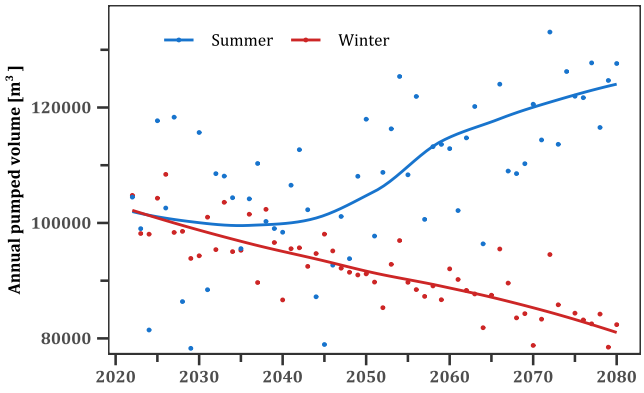

Fig. 6. Seasonal average extracted/injected volume from ATES wells associated with the thermal load. The lines represent local polynomial regression adjustments.

the seasonal volume plot (lines in Fig. 6). Employing the temperatures retrieved from the RCP8.5 projection after 60 years, we obtain an increase of 21.4% in cold water extraction and a decrease of 20.9% in warm water extraction. In contrast, the extracted volumes remain constant for scenario 1, which relies on a constant SAT after 2022.

3.3. Numerical modeling

The simulation was initiated in 1906 for each scenario, corresponding to the beginning of SAT data availability in Bordeaux. The urbanization in scenarios 3 and 4 is considered from 1990. The ATES operation runs from 2022 to 2082. The modeled temperature log before ATES operation in scenario 1 depicts a linear temperature increase following the geothermal gradient (Fig. 7). Nevertheless, the log highlights the influence of porous media thermal conductivity on heat transfer in the ground layers. It shows that the aquifer, with a thermal conductivity of $\lambda = 3.0\,\mathrm{W\,m^{-1}\,K^{-1}}$, has a higher heat transfer compared to the aquitard, which has a thermal conductivity of $\lambda = 2.0\,\mathrm{W\,m^{-1}\,K^{-1}}$. The shape of the temperature profile in scenario 1 remains constant before the start of ATES operation as this scenario does not consider any land use changes or climate variation.

Scenarios 2, 3, and 4 represent transient GST values and urbanization. Here, before ATES operation, the modeled shallow temperature logs above 90 m depth depict an increasingly pronounced C-shape with time. Below 90 m depth, the temperature increases linearly according to the geothermal gradient of 3.0 °C/100 m. This temperature log shape above 90 m is a typical signature of transient heat gain from the surface influenced by both historical SAT increase and surface urbanization (Blum et al., 2021; Bayer et al., 2019; Ferguson and Woodbury, 2004; Harris and Chapman, 1997). These logs highlight a depth-dependent temperature difference between the three scenarios, governed by the assumed GST value and particularly urbanization intensity started in 1990 for scenarios 3 and 4. The different transient GST values for each scenario lead to different average groundwater temperatures in the aquifer just before the ATES start-up. In 2021, in scenario 2, the average groundwater temperature in the aquifer is 15.0 °C, while in scenario 4, which has the highest urbanization level, it rises to 15.9 °C.

After ATES start-up, the model results show a seasonal temperature variation in both wells depending on the operation mode (Fig. 8a). The temperature difference $\Delta T = 5.0\,°\mathrm{C}$ is correctly reproduced with the software plug-in. During the first ten years of ATES operation, the groundwater temperature in both wells at aquifer depth decreases in all scenarios (Fig. 8b). This phase corresponds to establishing the disturbed thermal regime in the aquifer due to ATES operation starting with warm water injection (Fig. 8a). In contrast, starting with a cold water injection would generate an increased global trend during this initial time. Then, scenario 1 illustrates temperature stabilization in the aquifer for both wells, indicating a pseudo-steady-state thermal regime throughout the operation.

For the three other scenarios (2, 3 and 4), the temperature in the aquifer at both wells follows similar trends, with a temperature shift due to the initial temperature influenced by urbanization intensity. During the initial phase, from 10 to 35 years of operation, there is a modest average temperature rise of 0.028 °C/y. After 35 years, the rate of temperature increase is 2.5 times faster, reaching 0.074 °C/y. These two distinct trends result from the SAT (Fig. 3) trend assumed for these three scenarios, influencing heat transfer from the surface and well operation.

At the aquifer scale, during the first five years of operation, the warm and cold thermal plumes created by the injection have a similar extension in all scenarios (Fig. 9). The isolines of +1.5 and −1.5 °C compared to the initial state before the operation are used to assess the extension of the thermal plumes. During the initial period, the +1.5 °C contour is slightly more extended than the −1.5 °C contour.

After this initial period, scenarios 2, 3, and 4 depict a pronounced warm plume that expands during ATES operation, while the cold storage decreases. This leads to warming of the aquifer, which increases with the urbanization intensity. The warm plume extension reaches almost 100 m around the wells after 35 years of operation, while the cold plume extension is lower than 25 m around the well for these three scenarios. This highlights the issue of cold water availability for the ATES system, illustrated by the lack of cold water storage after 35 years of operation, even at the end of a supposed cold water injection period.

On the contrary, scenario 1 depicts a similar extension of warm and cold thermal plumes. Here, a balanced availability of cold and warm water through the operation of the ATES is achieved. Scenario 1 delineates a proper operation of the ATES throughout its lifetime, consistent with theoretical ATES operation principles Fig. 1. The temperature of the cold and warm water at the end of the exploitation is around 12.6 °C and 19.2 °C, while the mean temperature above 90 m is 16.2 °C (Fig. 10).

The other scenarios characterize unbalanced systems, associated with a higher temperature of the plumes. For example, scenario 4 presents a cold water temperature of 16.1 °C, which is close to the mean temperature in the aquifer and which reveals a lack of cold storage (Fig. 10). Moreover, these scenarios depict a pronounced warming of the close surface layers compared to scenario 1. Combined with the pumping dynamic of each scenario, the thermal dynamics depicted in the previous paragraphs lead to different ATES performances (Fig. 11).

After a slight increase during the initial period, scenario 1 reveals a stable performance η_e of 0.85 at each well (Fig. 11a). This performance is due to a balanced pumping/injection rate R_V (Fig. 11b) and a similar extension of the thermal plume allowing a stable thermal recovery R_T through the operation (Fig. 11c).

In scenarios 2, 3, and 4, the performance of the wells also follows a slight increase during the initial period. Then, at the cold well, the performance is stable at around 0.8 during the first part of the operation. After that, η_e decreases sharply (Fig. 11a1), and the decrease occurs earlier with the development of urbanization (after 30 years for scenario 4 and 40 years for scenario 2). Despite an increase in R_V due to overpumping of the cold well, the warming of the aquifer does not allow the recovery of the cold injected water, indicated by the decrease of R_T after 20 years of operation. These two dynamics generate the collapse of the performance measured by η_e.

At the warm well, the performance does not stabilize after the initial period and starts to decrease after 10 years of operation (Fig. 11a2). The global warming of the aquifer allows a constant increase of R_T which is insufficient to offset the decline of R_V.

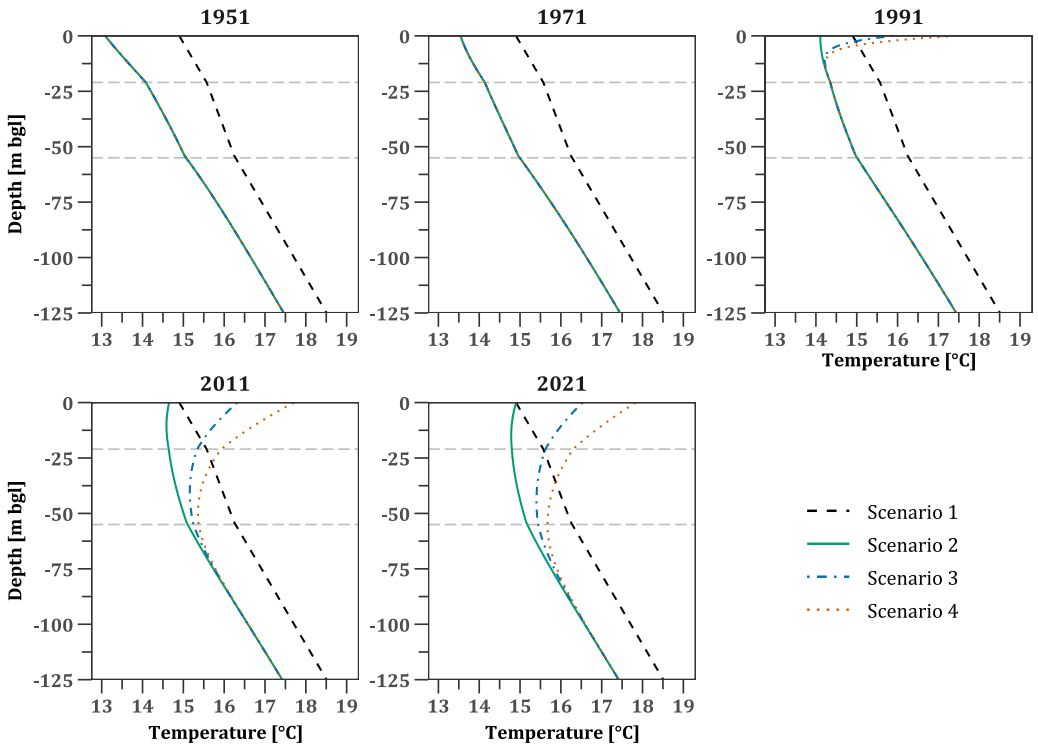

Fig. 7. Evolution of the modeled temperature profiles before ATES start-up (the horizontal lines represent the top and the bottom faces of the aquifer). bgl = Below ground level.

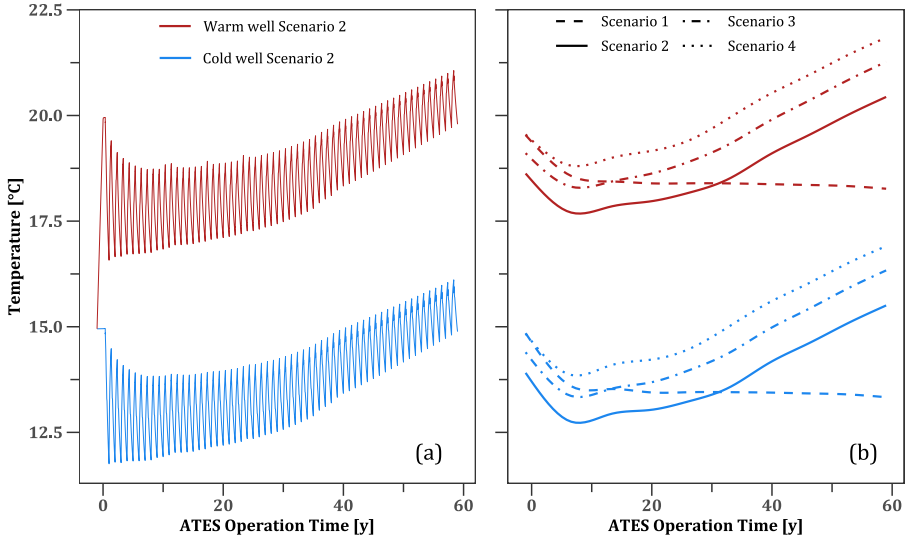

Fig. 8. Average transient groundwater temperature in ATES wells along the aquifer thickness: (a) temperature values retrieved from each modeled time-step of scenario 2 and (b) local polynomial regression for each scenario.

4. Discussion

In this study, scenario 1 represents the prevailing modeling methodology for ATES systems, considering a constant prescribed temperature at the upper face of the model, coupled with constant injection and extraction flow rates for both wells. The other investigated scenarios introduce transient thermal BCs at the surface considering changing SAT values due to climate change, and GST due to urbanization. In addition, we account for the evolution of building thermal regulation demand and adjusted flow rate influenced by SAT forecasts. Each modeled scenario replicates ATES operation, encompassing cold and warm storage dynamics within the aquifer. The thermal dynamics and the performance of the ATES system highly depend on the top thermal BCs. It is important to stress here that the thermal forcing by external factors is assumed to be significant in these scenarios. In more moderate conditions, the effects of ambient urban subsurface warming would be less pronounced.

The initial temperature distribution depicted in Fig. 7 denotes the necessity of considering the past historical events (urbanization development and past SAT) to accurately model the temperature distribution in the ground before ATES start-up. The common approach (scenario 1) reproduces a linear temperature log which is not representative of the

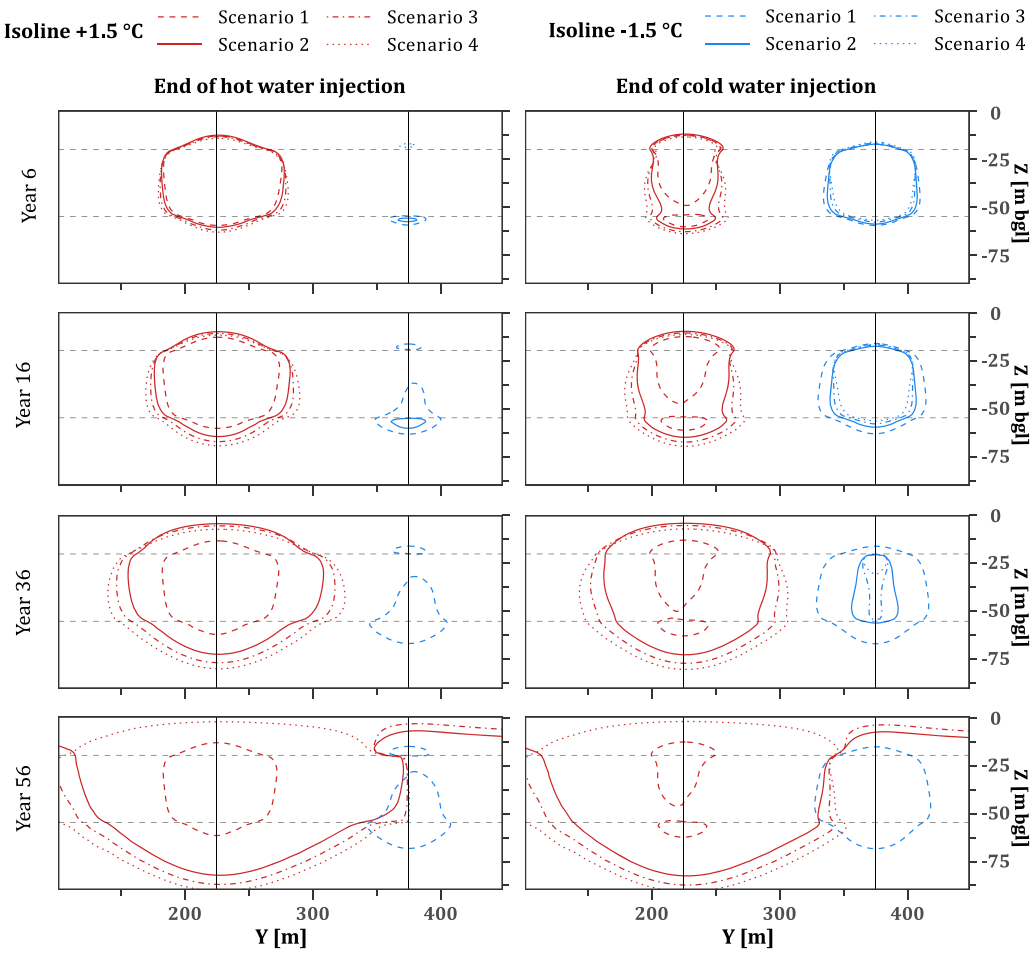

Fig. 9. Cross-section through ATES wells illustrating temperature difference at selected dates compared to the initial state just before the ATES start-up. The left panels represent the end of the warm water injection cycle and the right panels represent the end of the cold water injection. The dashed black horizontal lines demarcate the aquifer boundaries, and vertical lines represent the location of the wells.

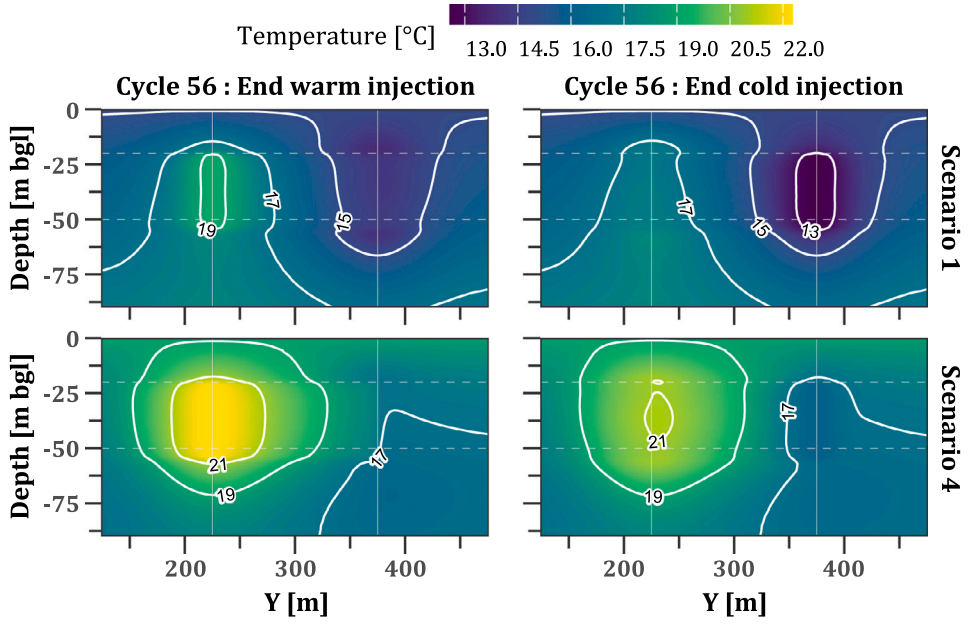

Fig. 10. Cross-section through ATES wells illustrating domain temperature and corresponding isothermal lines at the end of the ATES exploitation for scenarios 1 and 4. The left panels represent the end of the warm water injection cycle, and the right panels represents the end of the cold water injection. White horizontal dashed lines demarcate the aquifer, and vertical lines the wells.

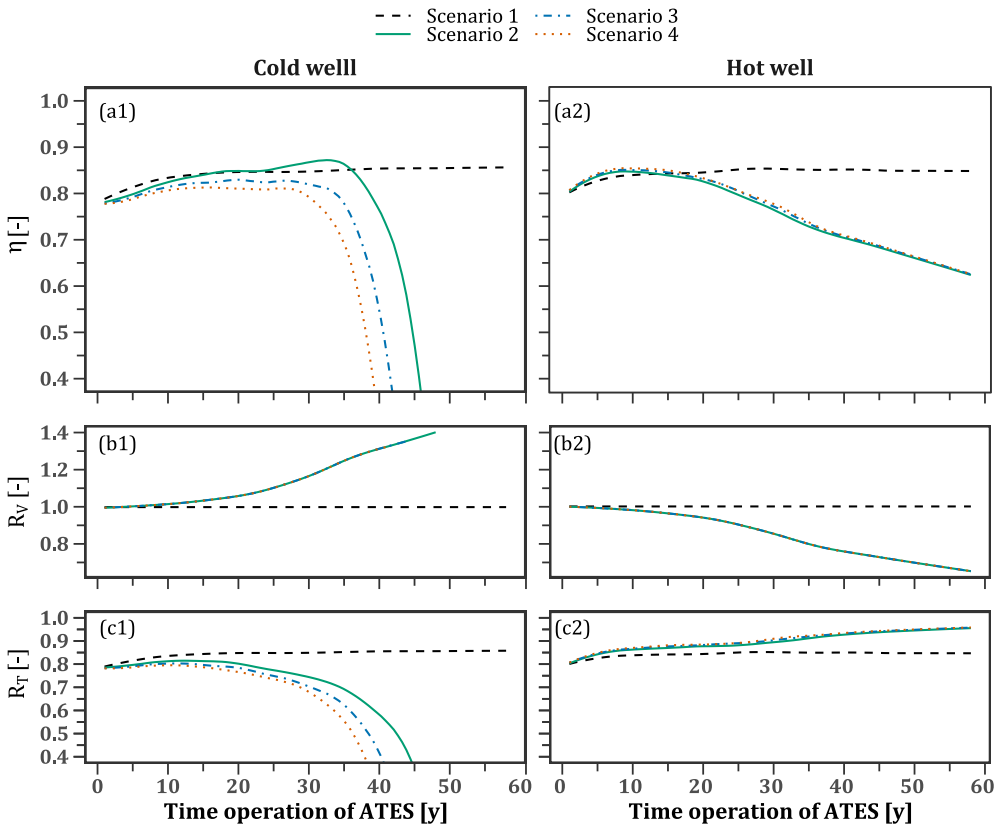

Fig. 11. Performance indicators of the ATES: (a) is the global performance of each well representing the combination of (b) the volumetric ratio of each well and (c) the thermal recovery of the wells.

thermal regime depicted in the shallow subsurface of cities. The other scenarios reproduce a temperature log with a C-shape above a depth of 90 m, which is characteristic of shallow (<100 m) urban subsurface influenced by urbanization and increasing SAT since the beginning of the 20th century. This strategy allows for the establishment of a more realistic thermal regime before the start-up of ATES.

In the context of a shallow ATES operation, scenario 1 exhibits stable performance alongside a balanced extension of the cold and warm plumes. However, the alternative scenarios depicted in this study underscore the importance of SAT forecasts and urbanization intensity as influential factors for ATES performance. These scenarios accentuate the necessity of incorporating such factors to prevent an overestimation of ATES performance in future projections.

Nevertheless, our study considers the RCP8.5 temperature projection in Bordeaux, while for instance, RCP6.0 could be considered more realistic on a worldwide scale. Compared to RCP8.5, RCP6.0 may decrease the building cooling load in the summer and increase the heating load in the winter. The unbalanced groundwater pumping may be lower than the one related to RCP8.5 (Fig. 6). Assuming RCP6.0 will also reduce the heat transfer from the atmosphere to the upper layers of the ground.

Comparison of scenarios 2, 3, and 4 illustrates the negative effects of urbanization on the efficiency of shallow ATES systems. Our study only considers the heat transfer from asphalt and buildings. The T_b value of 19.0 °C is in the upper scale of the likely value. This high value was chosen to compensate for the absence of sewage leakage and heat district consideration, which are non-negligible heat sources in urban grounds (Benz et al., 2015). With a lower T_b value, the negative effect on the aquifer warming could be reduced, and the ATES performance would be less affected.

To mitigate surface heat transfer impacts, green spaces at ATES sites should be preserved or restored. Additionally, ATES wells targeting deeper aquifers may offer a viable solution to mitigate these effects. Nevertheless, as ATES systems aim to produce and store cold water, the targeting aquifer should not be too deep to exploit cold water. The findings of this study also encourage regional management strategies in cities (e.g., sharing of thermal production for different buildings in the same area or using a cooling tower to lower the water temperature re-injection in winter) to reach a thermal balance in the aquifer and mutually benefit from the storage.

Our study assumes a uniform effect of urbanization in scenarios 3 and 4, incorporating the combined role of buildings and asphalt. However, this approach overlooks the thermal impact of specific roads, parking areas, or buildings on the aquifer, despite their potentially significant influence on the temperature of the aquifer at locations with ATES wells. The presented approach thus simplifies local conditions and does not resolve urban structures. While these may need to be simulated for individual ATES management, the presented results average their role in order to reveal regional trends at the city scale.

Moreover, our study considers a simplified methodology to calculate building thermal load and a 100% heat pump mode in summer while ATES can operate using free cooling, which is more economical than the heat pump mode with forced cooling. Free cooling influences the amount of water extracted from the cold well and re-injected in the warm well in the summer and the ΔT. It may impact the value of the wells' performance and thermal plume extension. However, free cooling is not effective once the groundwater temperature in the cold well exceeds 16.0 °C. This limits free cooling operation in the most critical scenarios and therefore compromises the economic efficiency of ATES. Regarding the heat pump mode considered in this study, the COP is considered constant along the modeled period, while the groundwater temperature increases for scenarios 2, 3, and 4. This increase may raise the COP during winter and decrease it during summer (Luo and Ma, 2022; Todorov et al., 2020).

Table A.3
List of various factors to consider for calculating the thermal demand of a building in summer (ASHRAE, 1997, 2021). For the equation parameter values, please refer to Tables A.5 and A.6.

Factor	Equation	Parameters
Walls–Roof–Windows	$q = U \times A \times (T_{max} - T_i)$	U = Heat transfer coeff. ($W\,m^{-2}\,K^{-1}$) A = Area (m^2) T_i = Indoor temperature (°C) T_{out} = Max daily outdoor temperature (°C)
Ventilation	$q = 1.23 \times Q_{vent} \times (T_{max} - T_i)$	Q_{vent} = Air flow rate required for 1 person ($L\,s^{-1}$)
Window radiation	$q = A \times SC \times SCL$	A = Windows area (m^2 SC = Shading factor (–) SCL = Solar cooling load ($W\,m^{-2}$)
People	$q = N \times P_{occ} \times O$	N = Number of people (–) P_{occ} = Heat gain per people (W) O = Occupancy rate (–)
Miscellaneous equipment	$q = N \times P_{eq}$	N = Number of equipments (–) P_{eq} = Heat due to device (W)
Lighting	$q = A \times E_v \times \eta^{-1} \times H_e$ (Suszanowicz, 2017)	A = Floor area (m^2) E_v = Illuminance ($lm\,m^{-2}$) η = Luminous efficacy ($lm\,W^{-1}$) H_e = Heat emission coeff. ($W\,W^{-1}$)
Workstation	$q = N \times P_{po} \times A_{po} \times O$	N = Number of workstations (–) P_{po} = Heat gain per m^2 ($W\,m^{-2}$) A_{po} = Area of workstation (m^2) O = Occupancy rate (–)

Table A.4
List of various factors to consider for calculating the thermal demand of a building in winter (ASHRAE, 1997, 2021). For the equation parameter values, please refer to Table A.5.

Factor	Equation	Parameters
Slab	$q = \Pi \times F_s \times (T_i - T_{min})$	Π = Slab perimeter (m) F_s = Heat transfer coeff. ($W\,m^{-1}$) T_{min} = Minimum outdoor daily temperature (°C)
Murs-Toit-vitres	$q = U \times A \times (T_i - T_{min})$	See Table A.3
Ventilation	$q = 1.23 \times Q_{vent} \times (T_c - T_{ext})$	See Table A.3

The purpose of this study was to emphasize the influence of GST increase on ATES performance. We advocate for the consideration of these processes in site-specific ATES performance evaluation studies. Clearly, the systems installed at particular sites will depend on local aquifer characteristics and heterogeneities, which determine the shape and extension of thermal plumes as well as the resulting performance of an ATES system (Sommer et al., 2013; Visser et al., 2015; Bridger and Allen, 2014; Ferguson, 2007; Dehkordi and Schincariol, 2014). Therefore, the results presented here reveal crucial relationships that have been overlooked in most related studies. However, the derived quantitative estimates cannot be generalized to other sites without adjusting simulated ground heat flux, hydrogeological and technological characteristics that may differ strongly from the ones assumed here.

5. Conclusion

We investigated the performance of LT-ATES systems under the combined impacts of SUHI and climate change. GST simulations reveal that urban development and climate change markedly affect initial thermal conditions and long-term ATES operation, with ambient subsurface warming altering extraction rates over 60 years. Numerical modeling demonstrates distinct thermal dynamics, showing that shallow urban subsurface conditions and intensified urbanization degrade system performance. Strategies like preserving green spaces and optimizing well placement are essential to mitigate these effects and ensure efficiency. Future research should focus on integrated models to better capture urban subsurface thermal dynamics and the evolving thermal loads of buildings. This study provides crucial insights for designing resilient and efficient geothermal energy systems for urban areas under climate change.

CRediT authorship contribution statement

Godinaud Jérémy: Writing – original draft, Visualization, Software, Methodology, Formal analysis, Data curation, Conceptualization. **Pryet Alexandre:** Writing – original draft, Validation, Supervision, Methodology. **Bayer Peter:** Writing – review & editing. **Larroque François:** Validation, Supervision, Methodology, Conceptualization.

Declaration of competing interest

The authors declare that they have no known competing financial interests or personal relationships that could have appeared to influence the work reported in this paper.

Acknowledgments

P. Bayer acknowledges financial support from the SpeicherCity project (03G0911H), funded by the Federal Ministry of Education and Research (BMBF). We would like to thank Ryan Pearson for his proofreading assistance and the two reviewers for their valuable contributions in improving the manuscript.

Appendix. Detail of the building thermal load calculation

The building thermal load in summer is the sum of each daily q detailed in Table A.3. For the winter thermal load, please refer to Table A.4. The target indoor temperature is 25 °C in summer and 20 °C in winter.

Table A.5
Building material properties (For the units, please refer to the Tables A.3 and A.4).

External loads		
Component	Properties	References
Roof	U = 0.33 Length = 150 Width = 100	Roof with a good thermal insulation
Wall N and S	U = 0.33 Length = 150.0 Height = 3.0	Roof with a good thermal insulation
Wall E and W	U = 0.33 Length = 100.0 Height = 3.0	Roof with a good thermal insulation
Windows N	U = 1.71 , SC = 0.3, A = 75 SCL = 115–150–118–109– 90 May/June/July/August/Sept	ASHRAE (1997) (Table 5, 11 Chap.29, Table 36.D Chap.28)
Windows S	U = 1.71, SC = 0.3, A = 75 SCL = 420–366–407–525–671 May/June/July/August/Sept	ASHRAE (1997) (Table 5, 11 Chap.29, Table 36.D Chap.28)
Windows E and W	U = 1.71 , SC = 0.3, A = 50 SCL = 697/684/684/681/630 May/June/July/August/Sept	ASHRAE (1997) (Table 5, 11 Chap.29, Table 36.D Chap.28)
Slab	F_s = 1.63 Length = 150 Width = 100	ASHRAE (2021) (Table 24 Chap.18)

Table A.6
Parameter specifications for description of internal heat gains.

Internal loads (only for cooling calculation)		
Factor	Characteristics	References
Occupancy	N = 652 P_{occ} = 117 W O = 0.7	ASHRAE (2021) (Table 1 Chap.18)
Workstations	N = 652 $P_{po} = 0.69\,\mathrm{W\,m^{-2}}$ $A_{po} = 11.5\,\mathrm{m^2}$ O = 0.7	Workstation : 1 laptop per station + 2 screens + 1 printer for 10 stations ASHRAE (2021) (Table 11 Chap.18)
Lighting	$A = 15\,000\,\mathrm{m^2}$ $E_v = 500\,\mathrm{lm/m^2}$ η = 140 lm W^{-1} H_e = 0.08 W W^{-1}	References for LED and E_v for office lighting Suszanowicz (2017)
Miscellaneous equipment	5 Coffee makers (P_{eq} = 376 W) 5 Microwaves oven (P_{eq} = 700 W) 5 Fridges (P_{eq} = 400 W) 5 Vending machines (P_{eq} = 600 W) 10 Projectors (P_{eq} = 300) 10 Speakers (P_{eq} = 15 W)	ASHRAE (2021) (Table 10 Chap.18)
Ventilation	$Q_{vent} = 7.0\,\mathrm{L\,s^{-1}}$ person^{-1}	Vandevyver and Pomian (2013)

Data availability

Data will be made available on request.

References

Alves, C.A., Gonçalves, F.L.T., Duarte, D.H.S., 2021. The recent residential apartment buildings' thermal performance under the combined effect of the global and the local warming. Energy Build. 238, 110828. http://dx.doi.org/10.1016/j.enbuild.2021.110828.

Arola, T., Korkka-Niemi, K., 2014. The effect of urban heat islands on geothermal potential: examples from Quaternary aquifers in Finland. Hydrogeol. J. 22 (8), 1953–1967. http://dx.doi.org/10.1007/s10040-014-1174-5.

ASHRAE, 1997. 1997 ASHRAE Handbook: Fundamentals.

ASHRAE, 2021. 2021 ASHRAE Handbook – Fundamentals. Ashrae.

Attard, G., Rossier, Y., Winiarski, T., Eisenlohr, L., 2016. Deterministic modeling of the impact of underground structures on urban groundwater temperature. Sci. Total Environ. 572, 986–994. http://dx.doi.org/10.1016/j.scitotenv.2016.07.229.

Banks, D., 2012. An Introduction to Thermogeology: Ground Source Heating and Cooling, second ed. John Wiley & Sons, Ltd, Hoboken, NJ.

Baxter, G., Srisaeng, P., Wild, G., 2018. An assessment of airport sustainability, Part 2—Energy management at copenhagen airport. Resources 7 (2), 32. http://dx.doi.org/10.3390/resources7020032.

Bayer, P., Attard, G., Blum, P., Menberg, K., 2019. The geothermal potential of cities. Renew. Sustain. Energy Rev. 106, 17–30. http://dx.doi.org/10.1016/j.rser.2019.02.019.

Bayer, P., Rivera, J.A., Schweizer, D., Schärli, U., Blum, P., Rybach, L., 2016. Extracting past atmospheric warming and urban heating effects from borehole temperature profiles. Geothermics 64, 289–299. http://dx.doi.org/10.1016/j.geothermics.2016.06.011.

Behi, M., Mirmohammadi, S.A., Suma, A.B., Palm, B.E., 2014. Optimized Energy Recovery in Line With Balancing of an ATES. American Society of Mechanical Engineers, Baltimore, Maryland, USA, V002T09A002. http://dx.doi.org/10.1115/POWER2014-32017.

Benz, S.A., Bayer, P., Menberg, K., Jung, S., Blum, P., 2015. Spatial resolution of anthropogenic heat fluxes into urban aquifers. Sci. Total Environ. 524–525, 427–439. http://dx.doi.org/10.1016/j.scitotenv.2015.04.003.

Benz, S.A., Menberg, K., Bayer, P., Kurylyk, B.L., 2022. Shallow subsurface heat recycling is a sustainable global space heating alternative. Nat. Commun. 13 (1), 3962. http://dx.doi.org/10.1038/s41467-022-31624-6.

Bidarmaghz, A., Choudhary, R., Narsilio, G., Soga, K., 2021. Impacts of underground climate change on urban geothermal potential: Lessons learnt from a

case study in London. Sci. Total Environ. 778, 146196. http://dx.doi.org/10.1016/j.scitotenv.2021.146196, URL: https://linkinghub.elsevier.com/retrieve/pii/S0048969721012638.

Bloemendal, M., Hartog, N., 2018. Analysis of the impact of storage conditions on the thermal recovery efficiency of low-temperature ATES systems. Geothermics 71, 306–319. http://dx.doi.org/10.1016/j.geothermics.2017.10.009.

Bloemendal, M., Olsthoorn, T., 2018. ATES systems in aquifers with high ambient groundwater flow velocity. Geothermics 75, 81–92. http://dx.doi.org/10.1016/j.geothermics.2018.04.005.

Bloemendal, M., Olsthoorn, T., Van De Ven, F., 2015. Combining climatic and geo-hydrological preconditions as a method to determine world potential for aquifer thermal energy storage. Sci. Total Environ. 538, 621–633. http://dx.doi.org/10.1016/j.scitotenv.2015.07.084.

Blum, P., Menberg, K., Koch, F., Benz, S.A., Tissen, C., Hemmerle, H., Bayer, P., 2021. Is thermal use of groundwater a pollution? J. Contam. Hydrol. 239, 103791. http://dx.doi.org/10.1016/j.jconhyd.2021.103791.

Bozkaya, B., Li, R., Zeiler, W., 2018. A dynamic building and aquifer co-simulation method for thermal imbalance investigation. Appl. Therm. Eng. 144, 681–694. http://dx.doi.org/10.1016/j.applthermaleng.2018.08.095.

Bridger, D.W., Allen, D.M., 2014. Influence of geologic layering on heat transport and storage in an aquifer thermal energy storage system. Hydrogeol. J. 22 (1), 233–250. http://dx.doi.org/10.1007/s10040-013-1049-1.

Bulté, M., Duren, T., Bouhon, O., Petitclerc, E., Agniel, M., Dassargues, A., 2021. Numerical modeling of the interference of thermally unbalanced aquifer thermal energy storage systems in Brussels (Belgium). Energies 14 (19), 6241. http://dx.doi.org/10.3390/en14196241.

Ciancio, V., Salata, F., Falasca, S., Curci, G., Golasi, I., De Wilde, P., 2020. Energy demands of buildings in the framework of climate change: An investigation across Europe. Sustain. Cities Soc. 60, 102213. http://dx.doi.org/10.1016/j.scs.2020.102213.

Dědeček, P., Šafanda, J., Rajver, D., 2012. Detection and quantification of local anthropogenic and regional climatic transient signals in temperature logs from Czechia and Slovenia. Clim. Change 113 (3–4), 787–801. http://dx.doi.org/10.1007/s10584-011-0373-5.

Dehkordi, S.E., Schincariol, R.A., 2014. Effect of thermal-hydrogeological and borehole heat exchanger properties on performance and impact of vertical closed-loop geothermal heat pump systems. Hydrogeol. J. 22 (1), 189–203. http://dx.doi.org/10.1007/s10040-013-1060-6, URL: http://link.springer.com/10.1007/s10040-013-1060-6.

Epting, J., Michel, A., Affolter, A., Huggenberger, P., 2021. Climate change effects on groundwater recharge and temperatures in Swiss alluvial aquifers. J. Hydrol. X 11, 100071. http://dx.doi.org/10.1016/j.hydroa.2020.100071, URL: https://www.sciencedirect.com/science/article/pii/S2589915520300225.

Ferguson, G., 2007. Heterogeneity and thermal modeling of ground water. Ground Water 45, 485–490. http://dx.doi.org/10.1111/j.1745-6584.2007.00323.x.

Ferguson, Woodbury, 2004. Subsurface heat flow in an urban environment: Subsurface URBAN heat flow. J. Geophys. Res. 109 (B2), http://dx.doi.org/10.1029/2003JB002715.

Fleuchaus, P., Schüppler, S., Godschalk, B., Bakema, G., Blum, P., 2019. Performance analysis of aquifer thermal energy storage (ATES). Renew. Energy 146, 1536–1548. http://dx.doi.org/10.1016/j.renene.2019.07.030.

Gao, L., Zhao, J., An, Q., Wang, J., Liu, X., 2017. A review on system performance studies of aquifer thermal energy storage. Energy Procedia 142, 3537–3545. http://dx.doi.org/10.1016/j.egypro.2017.12.242.

Godinaud, J., 2023. Le Dispositif De Stockage Saisonnier en Aquifère (ATES) de Faible Profondeur : Application au Domaine Urbain en Contexte de Changement Climatique (Ph.D. thesis). (2023BOR30014), Université Michel de Montaigne - Bordeaux III, URL: https://theses.hal.science/tel-04198473.

Godinaud, J., Loubet, P., Gombert-Courvoisier, S., Pryet, A., Dupuy, A., Larroque, F., 2024. Life cycle assessment of an aquifer thermal energy storage system: Influence of design parameters and comparison with conventional systems. Geothermics 120, 102996. http://dx.doi.org/10.1016/j.geothermics.2024.102996.

Harris, R.N., Chapman, D.S., 1997. Borehole temperatures and a baseline for 20th-century global warming estimates. Science 275 (5306), 1618–1621. http://dx.doi.org/10.1126/science.275.5306.1618.

Herb, W.R., Janke, B., Mohseni, O., Stefan, H.G., 2008. Ground surface temperature simulation for different land covers. J. Hydrol. 356 (3–4), 327–343. http://dx.doi.org/10.1016/j.jhydrol.2008.04.020.

Huang, S., Pollack, H.N., Shen, P.-Y., 2000. Temperature trends over the past five centuries reconstructed from borehole temperatures. Nature 403 (6771), 756–758. http://dx.doi.org/10.1038/35001556, URL: https://www.nature.com/articles/35001556.

Jalali, Z., Shamseldin, A.Y., Ghaffarianhoseini, A., 2023. Impact assessment of climate change on energy performance and thermal load of residential buildings in New Zealand. Build. Environ. 243, 110627. http://dx.doi.org/10.1016/j.buildenv.2023.110627.

Kranz, S., Frick, S., 2013. Efficient cooling energy supply with aquifer thermal energy storages. Appl. Energy 109, 321–327. http://dx.doi.org/10.1016/j.apenergy.2012.12.002.

Luo, J., Ma, X., 2022. An integrated strategy for the improvement of thermo-economic performance of a GWHP system. Appl. Therm. Eng. 213, 118777. http://dx.doi.org/10.1016/j.applthermaleng.2022.118777.

Ma, R., Zheng, C., 2010. Effects of density and viscosity in modeling heat as a groundwater tracer. Groundwater 48 (3), 380–389. http://dx.doi.org/10.1111/j.1745-6584.2009.00660.x.

Moulopoulos, A., 2014. Life Cycle Assessement of an Aquifer Thermal Energy Storage system (Ph.D. thesis). Utrecht University, URL: https://studenttheses.uu.nl/handle/20.500.12932/18918.

Noethen, M., Hemmerle, H., Bayer, P., 2023. Sources, intensities, and implications of subsurface warming in times of climate change. Crit. Rev. Environ. Sci. Technol. 53 (5), 700–722. http://dx.doi.org/10.1080/10643389.2022.2083899.

Previati, A., Epting, J., Crosta, G.B., 2022. The subsurface urban heat island in Milan (Italy) - A modeling approach covering present and future thermal effects on groundwater regimes. Sci. Total Environ. 810, 152119. http://dx.doi.org/10.1016/j.scitotenv.2021.152119, URL: https://linkinghub.elsevier.com/retrieve/pii/S0048969721071953.

Reveshti, A.M., Ebrahimpour, A., Razmara, J., 2023. Investigating the effect of new and old weather data on the energy consumption of buildings affected by global warming in different climates. Int. J. Thermofluids 19, 100377. http://dx.doi.org/10.1016/j.ijft.2023.100377.

Rivera, J.A., Blum, P., Bayer, P., 2015. Analytical simulation of groundwater flow and land surface effects on thermal plumes of borehole heat exchangers. Appl. Energy 146, 421–433. http://dx.doi.org/10.1016/j.apenergy.2015.02.035.

Rostampour, V., Jaxa-Rozen, M., Bloemendal, M., Kwakkel, J., Keviczky, T., 2019. Aquifer thermal energy storage (ATES) smart grids: Large-scale seasonal energy storage as a distributed energy management solution. Appl. Energy 242, 624–639. http://dx.doi.org/10.1016/j.apenergy.2019.03.110.

Schüppler, S., Fleuchaus, P., Blum, P., 2019. Techno-economic and environmental analysis of an aquifer thermal energy storage (ATES) in Germany. Geotherm. Energy 7 (1), 11. http://dx.doi.org/10.1186/s40517-019-0127-6.

Sommer, W., Valstar, J., Van Gaans, P., Grotenhuis, T., Rijnaarts, H., 2013. The impact of aquifer heterogeneity on the performance of aquifer thermal energy storage: Thermal energy storage and heterogeneity. Water Resour. Res. 49 (12), 8128–8138. http://dx.doi.org/10.1002/2013WR013677.

Stemmle, R., Blum, P., Schüppler, S., Fleuchaus, P., Limoges, M., Bayer, P., Menberg, K., 2021. Environmental impacts of aquifer thermal energy storage (ATES). Renew. Sustain. Energy Rev. 151, 111560. http://dx.doi.org/10.1016/j.rser.2021.111560.

Suszanowicz, D., 2017. Internal heat gain from different light sources in the building lighting systems. In: Wzorek, M., Królczyk, G., Król, A. (Eds.), E3S Web Conf. 19, 01024. http://dx.doi.org/10.1051/e3sconf/20171901024.

Taylor, C.A., Stefan, H.G., 2009. Shallow groundwater temperature response to climate change and urbanization. J. Hydrol. 375 (3–4), 601–612. http://dx.doi.org/10.1016/j.jhydrol.2009.07.009.

Todorov, O., Alanne, K., Virtanen, M., Kosonen, R., 2020. A method and analysis of aquifer thermal energy storage (ATES) system for district heating and cooling: A case study in Finland. Sustain. Cities Soc. 53, 101977. http://dx.doi.org/10.1016/j.scs.2019.101977.

Vandevyver, B., Pomian, J.-L., 2013. Fiche Pratique de Sécurité ED 23 - L'aménagement des bureaux. Technical Report, INRS, URL: https://www.inrs.fr/media.html?refINRS=ED%2023.

Vanhoudt, D., Desmedt, J., Van Bael, J., Robeyn, N., Hoes, H., 2011. An aquifer thermal storage system in a Belgian hospital: Long-term experimental evaluation of energy and cost savings. Energy Build. 43 (12), 3657–3665. http://dx.doi.org/10.1016/j.enbuild.2011.09.040.

Visser, P.W., Kooi, H., Bense, V., Boerma, E., 2020. Impacts of progressive urban expansion on subsurface temperatures in the city of Amsterdam (The Netherlands). Hydrogeol. J. 28 (5), 1755–1772. http://dx.doi.org/10.1007/s10040-020-02150-w, URL: https://link.springer.com/10.1007/s10040-020-02150-w.

Visser, P.W., Kooi, H., Stuyfzand, P.J., 2015. The thermal impact of aquifer thermal energy storage (ATES) systems: a case study in the Netherlands, combining monitoring and modeling. Hydrogeol. J. 23 (3), 507–532. http://dx.doi.org/10.1007/s10040-014-1224-z.

Watson, S.M., Westaway, R., 2020. Borehole temperature log from the Glasgow Geothermal Energy Research Field Site: a record of past changes to ground surface temperature caused by urban development. SJG 56 (2), 134–152. http://dx.doi.org/10.1144/sjg2019-033.